# Estimating the internal and surface oxidation of soot agglomerates

# Estimating the internal and surface oxidation of soot agglomerates

*Georgios A. Kelesidis and Sotiris E. Pratsinis\**

Particle Technology Laboratory, Institute of Process Engineering,

Department of Mechanical and Process Engineering, ETH Zürich,

Sonneggstrasse 3, CH-8092 Zürich, Switzerland.

Ph. +41 (0) 44 632 31 80; Fax. +41 (0) 44 632 15 95

*Corresponding author: pratsinis@ethz.ch

**Abstract**

Oxidation of soot takes place inside and on the surface of its constituent primary particles at a rate that depends on temperature, $T$, and $O_2$ concentration. Even though accurate oxidation kinetics are essential in both industrial uses and environmental impact of soot, they are often derived neglecting internal particle oxidation and the structure of such soot agglomerates. Here, the detailed evolution of the fractal-like agglomerate soot mass, $m$, and mobility diameter, $d_m$, during both internal and surface oxidation is determined by a moving sectional model. The model predictions are in excellent agreement with oxidation data of mature ethylene soot $d_m$ for $T = 900 - 1200$ K. The oxidation mode index, $a$, given by the ratio of the characteristic $O_2$ reaction and diffusion times is used to quantify the contributions of internal and surface oxidation of soot. At low $T$ (e.g., < 1100 K), $O_2$ diffuses into the primary particles and reacts with bulk soot, hardly altering the $d_m$ and yielding $a > 3$. As $T$ increases, surface oxidation becomes dominant, decreasing both $d_m$ and $a$. The common assumption that soot agglomerates are spheres underestimates their $d_m$ up to 50 % during oxidation. Coupling this detailed moving sectional model with soot mobility size distributions can yield realistic soot oxidation rates. Accounting for soot morphology and internal oxidation shows that the classic NSC rate increasingly underestimates (by 3 to 7 times) the oxidation rate of soot (from ethylene and toluene flames) with decreasing temperature (900-1800 K) and/or oxygen concentration (0.2 – 21 vol. %).

## 1. Introduction

Oxidation of soot and carbon blacks determines their emitted mass concentration and production rate as well as mobility, $d_m$, and primary particle diameters, $d_p$. Soot oxidation takes place mostly by $O_2$ and OH radicals at high temperatures, $T$ (> 1100 K) and competes with agglomeration in determining its particle sizes. In diesel engine exhaust and regenerative traps of particulate filters, single or packed beds of soot agglomerates are oxidized at lower temperatures [1]. Accurate soot oxidation rates over a wide temperature range are essential to design efficient and clean combustion processes.

At low $T$ (600-1100 K), $O_2$ diffuses into the primary particles and reacts with bulk soot. This results in combustion and rearrangement of the polyaromatic hydrocarbons (PAHs) constituting the soot primary particles [2], increasing their porosity and internal surface area [3]. Hollow primary particles of diesel [4] or biodiesel soot [5] and different carbon black grades [6, 7] are formed by extensive internal oxidation, while their $d_p$ [3] and agglomerate $d_m$ [8] are hardly altered. As $T$ increases, surface oxidation becomes gradually dominant, removing PAHs from the primary particle perimeter and decreasing both $d_p$ [3] and $d_m$ [8]. The fractal-like structure of soot agglomerates (e.g., $d_m$ < 135 nm [9]) can be preserved during oxidation. However, larger agglomerates may break into smaller ones [10] increasing the total number concentration of soot [11].

The mature carbon black oxidation rate by Nagle & Strickland-Constable (NSC) [12] was one of the first rates proposed for high temperatures and is still widely-used even for nascent soot nanoparticles. However, the NSC oxidation rate may underpredict up to 40 times the soot oxidation rate [13], as mature carbon black is much less reactive than nascent soot agglomerates [14]. For this, Puri et al. [15] and Xu et al. [16] sampled soot nanoparticles thermophoretically from diffusion flames and measured the decrease of soot $d_p$ with increasing height above the burner by oxidation using microscopy images. The derivation of

oxidation rates during soot formation relies on the accuracy of measured oxidative gaseous species in order to distinguish between oxidation by $O_2$ and OH radicals [15].

Thermogravimetric analysis (TGA) has been used instead to better control the concentration of oxidative gaseous species and study a wider temperature range [17]. There, $O_2$ flows over a packed bed of soot particles and the oxidation rate is measured by monitoring the bed mass lost by oxidation as a function of time [17]. The TGA-derived oxidation rates may neglect inter- and intraparticle $O_2$ diffusion limitations through the packed bed [18]. Oxidative flames [19] and flow reactors have been used to study the oxidation of single nascent [14] and mature ethylene [20] or diesel soot agglomerates [21] in the absence of interparticle mass-transfer limitations. The soot agglomerate mobility diameter is measured before and after oxidation by a scanning mobility particle sizer. The oxidized mass is typically estimated assuming that soot agglomerates are either spheres [19-21] and/or cylinders [14]. Furthermore, internal oxidation is typically neglected, even though it consumes most of soot mass for $T < 1050$ K [8] and is the dominant mechanism for cleaning diesel particulate filters. So, detailed models accounting for both internal and surface oxidation of soot agglomerates are needed.

Surface soot oxidation has been simulated by sectional [22] and moment models [23] by reducing uniformly soot $d_p$ and assuming that the agglomerate $d_m$ is equal to its diameter of gyration. Discrete element modeling of agglomeration and surface growth accounting for the detailed soot morphology showed that this assumption may underestimate the nascent soot $d_m$ up to 40 % and overestimate the mature soot $d_m$ up to 30 % [24]. The internal structure of soot primary particles is approximated by population balance models using cylindrical pores to elucidate the effect of oxidative fragmentation on soot number concentration [25] at different temperatures [26]. Kinetic Monte-Carlo simulations revealed that internal oxidation may increase the soot primary particle porosity [27]. However, the impact of internal oxidation on soot mass, $d_m$ and specific oxidation rate has not been quantified yet.

Here, the detailed evolution of fractal-like soot agglomerate mass and $d_m$ by internal and surface oxidation in the absence of fragmentation is described by developing a moving sectional model [28]. The oxidation mode index, $a$, given by the ratio of the characteristic $O_2$ reaction and diffusion times, relates the soot bulk density to $d_p$ [29] and is used to quantify the contributions of internal and surface oxidation of soot. A relationship for the $d_m$ of soot agglomerates formed by coagulation and surface growth [24] is used to account for their fractal-like morphology during internal and surface oxidation. The moving sectional model is benchmarked against mass and $d_m$ measurements of mature ethylene soot [8]. The specific oxidation rate of nascent ethylene soot is estimated accounting for internal and surface oxidation of agglomerates and compared to the classic NSC [12] rate and measurements of nascent ethylene soot size distributions after oxidation [14].

## 2. Theory

### 2.1. Soot agglomerate morphology

Soot agglomerates consist of polydisperse single and aggregated primary particles with geometric standard deviation of $1.2 \pm 0.01$ [30]. Their equivalent surface area mean primary particle diameter, $d_{va}$, and number, $n_{va}$, are [31]:

$$d_{va} = \frac{6m}{A_{ext} \cdot \rho} \tag{1}$$

$$n_{va} = \frac{m}{\rho \frac{\pi}{6} d_{va}^3} \tag{2}$$

where $m$, $A_{ext}$ and $\rho$ are the agglomerate mass, external surface area and bulk density, respectively. The $A_{ext,o}$ of soot agglomerates before oxidation is given by combining Eq. 1 and 2:

$$A_{ext,o} = n_{va,o} \pi d_{va,o}^2 \tag{3}$$

During surface oxidation, $A_{ext}$ is related to $m$ and $\rho$ by [32]:

4

$$\frac{A_{ext}}{A_{ext,o}} = \left(\frac{\rho_o m}{\rho \cdot m_o}\right)^{D_s/3} \tag{4}$$

where $D_s = 2.25 \pm 0.05$ is the surface fractal dimension describing the soot [30] and carbon

black surface roughness [33]. The soot fractal-like morphology can be quantified by [24]:

$$d_m = d_{va} n_{va}^{0.45} \tag{5}$$

Equation 5 (derived for soot agglomerates of polydisperse single and aggregated primary

particles formed by surface growth, aggregation and agglomeration [24]) is in excellent

agreement with mass-mobility data of soot from the CAST generator, diffusion [24] and

premixed flames [34] before and after oxidation at 973 K (Fig. S1). The latter indicates that

oxidation does not alter the fractal-like soot morphology, consistent with microscopy data [9].

*2.2. Internal structure of soot primary particles*

Soot primary particles are assumed to consist of cylindrical pores [25] with length, $l_{pore} = 1$

nm [35] and width, $d_{pore} = 0.2$ nm [36] formed between their constituent clusters of 4-5 PAHs

[25]. Then, the internal soot surface area before oxidation, $A_{int,o}$, is obtained by:

$$A_{int,o} = n_{va,o} n_{pore} \pi d_{pore} l_{pore} \tag{6}$$

where $n_{pore}$ is the number of pores per soot primary particle [25]:

$$n_{pore} = \theta_C \frac{\rho_o \frac{\pi}{6} d_{va,o}^3}{n_{CC}} \tag{7}$$

where $n_{CC} = 100$ is the number of carbon atoms per PAH cluster [25] and $\theta_c$ is the mass

fraction of carbon atoms per primary particle estimated using $\rho_o$ [37]:

$$\theta_C = \frac{0.26088 \rho_o b^2 c - w_H}{w_C - w_H} \tag{8}$$

where $b = 2.46$ Å is the graphite unit cell in the basal plane, $c = 3.53$ Å is the interlayer

spacing, while $w_C$ and $w_H$ are the atomic weights of carbon and hydrogen, respectively [37].

The initial soot primary particle porosity, $\varphi$, is given by the ratio of the total pore over the

primary particle volume:

$$\varphi = \frac{3 n_{pore} d_{pore}^2 l_{pore}}{2 d_{va,o}^3} \qquad (9)$$

At low temperatures and/or high $O_2$ concentrations, $O_2$ can diffuse through the soot pores, internally oxidizing the soot primary particles and reducing their initial $\rho_o$ by [29]:

$$\frac{\rho}{\rho_o} = \left( \frac{d_{va}}{d_{va,o}} \right)^a \qquad (10)$$

where $\alpha$ is the oxidation mode index given by Thiele analysis [29, 38]:

$$a = 3 \frac{A_{int,o} \rho_o}{2 m_o} \sqrt{\frac{[O_2] D_{O_2} d_{pore} w_C}{R_g T \omega}} \qquad (11)$$

where $R_g$ is the universal gas constant, $T$ is the temperature, $[O_2]$, $\omega$ and $D_{O2}$ are the $O_2$ concentration, specific oxidation rate and diffusivity in the bulk soot, respectively. Diffusion of $O_2$ in bulk soot takes place in the Knudsen regime [39] with $D_{O2}$ given by [40]:

$$D_{O_2} = \frac{4\phi}{3\tau} \sqrt{\frac{R_g T}{2\pi MW_{O_2}}} d_{pore} \qquad (12)$$

where $MW_{O2}$ is the $O_2$ molecular weight and $\tau = 14.4$ the soot primary particle tortuosity [41].

Figure 1 shows $a$ as function of $T$ for $[O_2] = 21$ (broken line), 2.1 (dot-broken line) and 0.21 vol % (solid line) estimated using Eq. 10 with $\omega$ derived by Nagle-Strickland-Constable (NSC) for mature carbon black [12] and $d_{va,o} = 16.7$ nm [8]. For $a = 3$ (dotted line), the characteristic $O_2$ reaction and diffusion times are identical [29] so the contributions of internal and surface oxidation to the total oxidized soot mass are comparable. At low $T$ and $\alpha > 3$, the characteristic $O_2$ diffusion time is smaller than its reaction time and the contribution of internal to total soot oxidation is much larger than that of surface oxidation. As $T$ increases, $a$ gradually decreases below 3, indicating that the contribution of internal oxidation decreases so surface oxidation dominates. Furthermore, as $[O_2]$ decreases from 21 (broken line) to 0.21 vol % (solid line), the transition from internal to surface-dominated oxidation shifts to lower $T$. At

6

higher [$O_2$], most of the active surface sites have been occupied or reacting with a small fraction of the available $O_2$. So, the rest, unreacted $O_2$ diffuses through the pores to find new active sites for reaction. The soot $A_{int}$ is inversely proportional to $\rho$, similarly to inorganic nanoparticles [42]. So, the decrease of soot $A_{int}$ is given by:

$$A_{int} = \frac{\rho_o}{\rho} A_{int,o} \qquad (13)$$

**Figure 1**

*2.3. Numerical implementation*

The evolution of soot agglomerate $m$ and $d_m$ distributions during internal and surface oxidation is investigated for $T = 900 - 1800$ K and [$O_2$] = 0.21 - 21 vol % using a moving sectional model [28]. The initial bulk density, $\rho_o$, of nascent and mature soot varies from 1500 to 1800 kg/m$^3$, respectively, in these simulations. The number of carbon atoms per PAH cluster, $n_{cc}$, is constant at 100, while the hydrogen atoms are reduced with increasing soot maturity [43]. So, nascent soot nanoparticles consist of clusters of 4 - 5 physically-bonded PAHs (e.g. perylene, coronene [44] or benzo[a]pyrene [45]). These PAH clusters have C/H = 1.67 - 2 resulting in $\rho_o$ = 1400 - 1500 kg/m$^3$ [37], consistent with that derived from mass-mobility data [46]. As nascent soot nanoparticles mature by dehydrogenation [43], their PAH clusters chemically-bond together increasing their $\rho_o$ and C/H up to 1800 kg/m$^3$ and 4.5, respectively. The initial soot $d_m$ distribution is discretized in 60 sections with $d_{m,i+1}/d_{m,i}$ = 1.7 [28] starting from 2 nm. The initial mass of each section is estimated from Eqs. 2 and 5 using a primary particle diameter of 7.5 nm [30] or 16.7 nm [8]. The initial soot primary particle diameter, $d_{va,o}$, depends on combustion conditions (e.g., equivalence ratio) and increases at higher soot volume fractions [30]. Soot agglomerates with small $d_{va,o}$ have larger $n_{va}$ and effective density than those with large $d_{va,o}$ and the same $d_m$ [34]. This increases their specific surface area, *SSA*, available for oxidation and results in fast reduction of their $d_m$ (Fig. S4). For example, after 0.1 s of oxidation at [$O_2$] = 21 vol % and $T = 1000$ K, agglomerates with

7

$d_{m,o}$ = 93 nm and $d_{va,o}$ = 8.5 nm have 10 % smaller $d_m$ than those with the same $d_{m,o}$ but $d_{va,o}$ = 16.7 nm. Thus, at short $t$, mobility measurements are not that sensitive to primary particle size at these combustion conditions. The model exhibits little sensitivity to $n_{cc}$, $l_{pore}$ and $d_{pore}$ variations up to 85 % of mass loss by oxidation at [$O_2$] = 21 vol % and $T$ = 1000-1800 K (Fig. S5). For each section $i$, the reduction of soot agglomerate $m$ by surface and internal oxidation is estimated as function of time, $t$, by:

$$\frac{dm_i}{dt} = -\omega\left(A_{ext,i} + \eta A_{int,i}\right)$$ (14)

where $\eta$ is the effectiveness factor [38]:

$$\eta = \frac{2m_o a}{A_{i,o}\rho_o d_{va,o}}\left(\coth\left(\frac{3A_{i,o}\rho_o d_{va,o}}{2m_o a}\right) - \frac{2m_o a}{3A_{i,o}\rho_o d_{va,o}}\right)$$ (15)

For $\eta$ = 1, $O_2$ fully penetrates primary particles, while for $\eta$ = 0 solely acts on their surface [36]. The agglomerate $A_{ext}$, $A_{int}$, $\rho$, $n_{va}$, $d_{va}$ and $d_m$ are estimated from its $m$ as function of $t$ using Eqs. 4, 12, 9, 1, 2 and 5, respectively. In the absence of fragmentation [11], the number concentration, $N$, of each section remains constant with $t$. Soot particles with $d_m \geq 2$ nm are modelled as solid single, aggregates or agglomerates of spheres, consistent with microscopy and mobility size measurements [47], as well as with discrete element modeling for soot surface growth and agglomeration [30]. Upon extensive oxidation, the soot agglomerate $d_m$ may drop below 2 nm. Atomic force microscopy revealed that soot particles with $d_m < 2$ nm consist a few polyaromatic hydrocarbons [48]. So, sections that have attained $d_m < 2$ nm after oxidation are eliminated implying phase transition to gaseous or liquid state.

The moving sectional model (Eqs. 1-15) is validated at limiting cases with simple analytical models for surface oxidation of single spheres [49]:

$$d_m = d_{m,o} - \frac{2\omega}{\rho_o}\Delta t$$ (16)

and agglomerates:

$$d_m = d_{m,o} - \frac{2\omega}{\rho_o} \frac{d_{m,o}}{d_{va,o}} \Delta t \tag{17}$$

Equation 17 is derived from Eqs. 2-4 and 14, using $\eta = 0$, $a = 0$, $\rho = \rho_o$ and $D_s = 2$ [23]. It should be noted that this $D_s$ is just a simplification that facilitates derivation of an analytical formula (eq. 17) for surface oxidation of agglomerates that is in excellent agreement to the moving sectional model using $D_s = 2$ as it should (Fig. S2) and even with $D_s = 2.25$ (Fig. S3). The realistic $D_s = 2.25$, describing the soot [30] and carbon black surface roughness [33] is used in the moving sectional model simulations of internal and surface oxidation. Soot agglomerates having the same $n_{va}$, $d_{va}$, $d_m$ and $\rho$ as those derived by the moving sectional model are generated by discrete element modeling (DEM) for surface growth, aggregation [30] and agglomeration [24] and shown in Figs. 2-5. For example, an exemplary DEM-derived agglomerate with $n_{va,o} = 45$, $d_{va,o} = 16.7$ nm, $d_{m,o} = 93$ nm and $\rho_o = 1800$ kg/m$^3$ is shown in Fig. 3 at $t = 0$ s, consistent with the initial conditions used in the moving sectional model. During surface oxidation at $T = 1800$ K and $[O_2] = 21$ vol %, the $n_{va}$, $d_{va}$, $d_m$ of the DEM-derived agglomerate are reduced according to Eqs. 1-15. In the presence of internal oxidation, $\rho$ is also reduced as a function of $t$, and quantified by the decreasing intensity/opacity of the DEM-derived agglomerate.

## 3. Results and Discussion

The surface and internal soot oxidation dynamics are elucidated for monodisperse soot agglomerates with $d_{m,o} = 93$ nm, $d_{va,o} = 16.7$ nm and $\rho_o = 1800$ kg/m$^3$ from a diffusion ethylene flame [8]. Soot agglomerate fragmentation by oxidation is negligible for $d_m < 135$ nm [10]. Figure 2 shows the evolution of a) $d_m$ and b) $m$ of soot agglomerates during internal and surface oxidation (solid lines) in comparison to those estimated by surface oxidation only of agglomerates (Eq. 17; dot-broken lines) and initially equivalent-mass spheres (Eq. 16; broken lines) at $T = 1200$ K and $[O_2] = 21$ vol % using $\omega = 6.7 \cdot 10^{-5}$ kg/(m$^2 \cdot$ s) estimated

from the classic NSC [12]. The soot agglomerate $d_m$ remains monodisperse during surface and internal oxidation, indicating that the present moving sectional model is not affected by numerical diffusion [50].

Initially ($t = 0$ s), the $d_m$ of spheres (broken line) is smaller than that of agglomerates having the same $m$ (solid and dot-broken lines) due to the compact shape of spheres. During surface oxidation alone, the $d_m$ and $m$ of spheres (broken lines) are decreasing slower than those of agglomerates (dot-broken lines) due to the large surface area of the latter, consistent with theory [30]. Accounting for both internal and surface oxidation (solid lines) results in a much faster reduction of $m$ and $d_m$. The characteristic $O_2$ reaction and diffusion times are comparable at these $T$ and $[O_2]$ yielding $\alpha = 1.9$. So, internal oxidation results in the reduction of soot bulk density [29], elucidated here by increasing the transparency of internally oxidized agglomerates (a: red inset).

**Figure 2**

Figure 3 shows the evolution of a) $m$ and b) $d_m$ of soot agglomerates during internal and surface oxidation at the conditions of Fig. 2 (solid lines) as well as for $T = 1800$ (dot-broken lines) and 1000 K (broken lines) and $[O_2] = 21$ vol % using $\omega$ = NSC for the same $d_{m,o}$, $d_{va,o}$ and $\rho_o$ shown in Fig. 2. At $T = 1800$ K the contribution of internal burning to the total oxidized soot mass is small compared to that of fast surface oxidation ($a = 0.2$). So, $O_2$ reacts at the agglomerate soot surface, reducing the diameter but also the number of constituent primary particles, $n_{va}$, from 45 down to 34. This decreases rapidly both agglomerate $m$ (a) and $d_m$ (b) with $t$ compared to those at $T = 1200$ K.

At lower $T$, surface oxidation becomes slower, allowing $O_2$ molecules to diffuse and react within the primary particles [36]. At even lower $T$ (e.g. 1000 K, broken lines), internal oxidation dominates ($a = 8.1$) removing gradually most of the soot $m$ from inside its primary particles and further delaying reduction of their $d_m$ compared to oxidation at higher $T$. Soot agglomerates attaining the same $d_m$ (e.g. 70 nm) by oxidation have identical $n_{va}$ regardless of

*T*. However, the specific surface area, *SSA*, of oxidized agglomerates with $d_m = 70$ nm is increased by internal oxidation from 251 to 1127 $m^2$/g as *T* is reduced from 1800 to 1000 K. This enhancement of soot *SSA* by internal oxidation is consistent with $N_2$ adsorption measurements of mature carbon black oxidized at $T = 900 - 1100$ K [18].

**Figure 3**

Figure 4 shows the soot agglomerate $d_m$ as function of its *m* after internal and surface oxidation (solid line) compared to those of agglomerates (dot-broken line) and spheres after surface oxidation alone (broken line) at $T = 900 - 1200$ K (top axis) using $\omega$ = NSC, which results in $a = 21.5 - 1.9$ (top abscissa). Soot particles with different morphology attain the same *m* by surface and/or internal oxidation at different *t*, as shown in Fig. 3. In practice, surface oxidation takes place at high *T* (> 1100 K) after soot formation, burning up to 90 % of the total soot during diesel combustion [1]. The remaining mature soot agglomerates are directed to the diesel exhaust where they are burnt internally at low *T* (< 1100 K) [1]. The surface oxidation model for spheres (broken line) underestimates the measured $d_m$ [8; squares] by 50 % on average over the whole *T* range, as with surface growth and agglomeration in the absence of oxidation [30]. This is due to the compact shape of spheres that underestimates the $d_m$ of soot agglomerates having the same *m* (Fig. 3).

Accounting for the fractal-like agglomerate morphology during surface oxidation (dot-broken line) improves substantially the agreement with data [8; squares] for $T > 1100$ K, but underestimates soot $d_m$ up to 24 % for lower *T*, as oxidation takes place mostly within soot primary particles [8]. Accounting for both internal and surface soot oxidation of agglomerates (solid line) results in good agreement with mature soot data [8; squares] over the whole *T* range. The largest deviation between the moving sectional model (solid line) and the data [8; squares] at $T = 1173$ K could be attributed to the low measurement resolution for small soot mass remaining after extensive oxidation [8] as well as the assumed constant pore sizes.

**Figure 4**

The underestimation of soot $d_m$ by neglecting internal oxidation and/or fractal-like soot morphology (Fig. 4) results in overestimation of the $\omega$ derived from the measured $d_m$. This is elucidated here for nascent ethylene and toluene soot agglomerates with $\rho_o$ = 1500 kg/m$^3$ [14] and $d_{va,o}$ = 7.5 nm [30]. Figure 5 shows normalized mobility size distributions of agglomerates before (a, e; $t$ = 0 s) and after 0.217 (b, c) or 0.203 s (d, f) of internal and surface oxidation at $T$ = 955 (b, c), 1010 (d) or 1016 K (f) and [O$_2$] = 0.32 (b) or 0.78 vol % (c, d, f) obtained by a moving sectional model (lines) in comparison to measurements of nascent ethylene [14; triangles] and toluene soot oxidation [14; circles]. All size distributions are normalized by the maximum number concentration, $N_{max}$. At $t$ = 0 s (a), soot nanoparticles form compact agglomerates of aggregates and single primary particles [51; blue-framed inset] by surface growth and agglomeration [3] having average $<d_m>$ = 11.8 nm and $\sigma_{g,m}$ = 1.49 [14; triangles] or $<d_m>$ = 22.9 nm and $\sigma_{g,m}$ = 1.89 [14; circles]. A lognormal size distribution with the same $<d_m>$ and $\sigma_{g,m}$ is used initially for soot oxidation simulations by the present moving sectional model (a: solid line).

The particle size distribution shifts to smaller sizes by oxidation depending on specific oxidation rate, $\omega$, while the particle number concentration, $N$, remains constant (b: lines) due to the absence of fragmentation [14]. Using $\omega$ = NSC for mature carbon black [12] results in $<d_m>$ = 11.4 (b: broken line) which is 35 % larger than the measured $<d_m>$ = 8.7 nm after 0.217 s at $T$= 955 K and [O$_2$] = 0.32 vol % [14; triangles]. Using a similar $\omega$ that was derived for mature soot oxidation [52] results in hardly any soot oxidation overestimating the oxidized nascent soot $<d_m>$ by 35 % (b: dot-broken lines). Camacho et al. [14] attributed this overestimation to the larger reactivity of nascent soot than that of mature soot or carbon black.

**Figure 5**

The nascent ethylene soot $\omega$ is varied to match the measured $<d_m>$ after internal and surface oxidation. This is the typical method used to derive $\omega$ from mobility size distribution measurements [14, 19-21] and is detailed in the SI (Section C). For example, surface

oxidation of spheres with $\omega = 10 \times$ NSC resulted in size distributions with similar $<d_m>$ but larger $\sigma_{g,m}$ than the measured ones [14: Fig. 3, left panel]. So, using this nascent soot oxidation $\omega$ [14] in the present model for oxidation of agglomerates underestimates nascent soot $<d_m>$ by 20 % (b: dotted lines). Accounting for the detailed fractal-like soot structure during internal and surface oxidation, the best agreement with the measured $<d_m>$ and $\sigma_{g,m}$ [14; triangles] is attained with $\omega = 6.9 \times$ NSC (solid line). For [$O_2$] = 0.2 – 0.78 vol % and $T$ = 1010 and 955 K, average $\omega$ ranging from 3.2 $\times$ NSC to 7.2 $\times$ NSC are derived by the present sectional model for soot oxidation, respectively (Figure S6 & S7). The underestimation of nascent ethylene soot $\omega$ by the NSC rate decreases down to 5.4 $\times$ NSC or 3.2 $\times$ NSC with increasing [$O_2$] (c) or $T$ (d). The latter is in good agreement with mature ethylene soot [8] and carbon black $\omega$ measurements [18]. So, increasing [$O_2$] and/or $T$ decreases nascent soot $<d_m>$ and reactivity, reducing the difference between nascent and mature soot $\omega$. This is consistent with microscopy and TGA measurements [7] showing that extensive internal oxidation of amorphous carbon (similar to nascent soot) results in mature, graphitic shells having high activation energy for oxidation. Nascent toluene soot is less reactive than ethylene soot probably due to its large C/H ratio [53], resulting in 15 % smaller $\omega$ for similar $T$ and [$O_2$] conditions (d, f). Thus, neglecting internal oxidation, as well as the fractal-like soot morphology underestimates the nascent ethylene and toluene soot oxidation rate, $\omega$, by 3 - 7 times (e.g. using the classic NSC rate) at [$O_2$] = 0.78 - 0.2 vol % at modest $T$ = 900 -1200 K.

## 4. Conclusions

Soot dynamics during simultaneous surface and internal oxidation are elucidated for the first time to our knowledge using a moving sectional model that accounts for the fractal-like soot agglomerate morphology. The oxidation mode index, $a$, given by the ratio of the characteristic $O_2$ reaction and diffusion times [29] is used to quantify the contributions of internal and surface oxidation of soot. At low $T$ (< 1100 K), $O_2$ diffuses into the primary particles and

reacts with bulk soot, hardly altering the $d_m$ and yielding $a > 3$. As $T$ increases, surface oxidation becomes gradually dominant, decreasing both $d_m$ and $a$.

The common assumption that soot agglomerates are spheres underestimates their $d_m$ up to 50 % during soot oxidation. Thus, a relationship for the $d_m$ of agglomerates formed by coagulation and surface growth [24] is used to account for their fractal-like morphology during internal and surface oxidation. This is in excellent agreement with oxidation data of mature ethylene soot $d_m$ for $T = 900 - 1200$ K [8]. Interfacing this detailed moving sectional model predictions for internal and surface oxidation of soot agglomerates with measured mobility size distributions of nascent soot yields a specific oxidation rate that is smaller than that obtained when neglecting internal oxidation and soot morphology at $[O_2] = 0.2 - 0.78$ vol % [14]. Thus, the moving sectional model developed here can be used in tandem with $d_m$ measurements to derive accurate soot oxidation kinetics for different soot maturities at a wide range of combustion conditions in tandem with mobility measurements, facilitating the design of efficient and clean combustion processes.

## 5. Acknowledgements

## 6. References:

[1] B.R. Stanmore, J.F. Brilhac, P. Gilot, Carbon 39 (2001) 2247-2268.
[2] R.H. Hurt, A.F. Sarofim, J.P. Longwell, Combust. Flame 95 (1993) 430-432.
[3] T. Ishiguro, N. Suzuki, Y. Fujitani, H. Morimoto, Combust. Flame 85 (1991) 1-6.
[4] K. Al-Qurashi, A.L. Boehman, Combust. Flame 155 (2008) 675-695.
[5] J.H. Song, M. Alam, A.L. Boehman, U. Kim, Combust. Flame 146 (2006) 589-604.
[6] T.A. Heckman, D.F. Harling, Rubber Chem. Technol. 39 (1966) 1-3.

[7] C.K. Gaddam, R.L. Vander Wal, X. Chen, A. Yezerets, K. Kamasamudram, Carbon 98 (2016) 545-556.

[8] X. Ma, C.D. Zangmeister, M.R. Zachariah, J. Phys. Chem. C 117 (2013) 10723-10729.

[9] H.J. Jung, D.B. Kittelson, M.R. Zachariah, Combust. Flame 136 (2004) 445-456.

[10] H. Ghiassi, I.C. Jaramillo, P. Toth, J.S. Lighty, Combust. Flame 163 (2016) 170-178.

[11] K.G. Neoh, J.B. Howard, A.F. Sarofim, Symp. (Int.) Combust. 20 (1985) 951-957.

[12] J. Nagle, R.F. Strickland-Constable, Proceedings of the Fifth Conference on Carbon, 5th Ed.; Pergamon Press: Oxford, U.K., 1 (1961) 154-164.

[13] R.L. Vander Wal, A.J. Tomasek, Combust. Flame 134 (2003) 1-9.

[14] J. Camacho, Y.J. Tao, H. Wang, Proc. Combust. Inst. 35 (2015) 1887-1894.

[15] R. Puri, R.J. Santoro, K.C. Smyth, Combust. Flame 97 (1994) 128-144.

[16] F. Xu, A.M. El-Leathy, C.H. Kim, G.M. Faeth, Combust. Flame 132 (2003) 43-57.

[17] M.L. Chan, K.N. Moody, J.R. Mullins, A. Williams, Fuel 66 (1987) 1694-1698.

[18] P. Gilot, F. Bonnefoy, F. Marcuccilli, G. Prado, Combust. Flame 95 (1993) 87-100.

[19] H. Ghiassi, I.C. Jaramillo, J.S. Lighty, Energy Fuels 30 (2016) 3463-3472.

[20] K.J. Higgins, H.J. Jung, D.B. Kittelson, J.T. Roberts, M.R. Zachariah, J. Phys. Chem. A 106 (2002) 96-103.

[21] K.J. Higgins, H.J. Jung, D.B. Kittelson, J.T. Roberts, M.R. Zachariah, Environ. Sci. Technol. 37 (2003) 1949-1954.

[22] E.K.Y. Yapp, D.P. Chen, J. Akroyd, S. Mosbach, M. Kraft, J. Camacho, H. Wang, Combust. Flame 162 (2013) 2569-2581.

[23] M.E. Mueller, G. Blanquart, H. Pitsch, Combust. Flame 156 (2009) 1143-1155.

[24] G.A. Kelesidis, E. Goudeli, S.E. Pratsinis, Carbon 121 (2017) 527-535.

[25] M. Sirignano, J. Kent, A. D'Anna, Energy Fuels 27 (2013) 2303-2315.

[26] M. Sirignano, H. Ghiassi, A. D'Anna, J.S. Lighty, Combust. Flame 171 (2016) 15-26.
[27] M. Frenklach, Z.Y. Liu, R.I. Singh, G.R. Galimova, V.N. Azyazov, A.M. Mebel, Combust. Flame 188 (2018) 284-306.

[28] P.T. Spicer, O. Chaoul, S. Tsantilis, S.E. Pratsinis, J. Aerosol Sci. 33 (2002) 17-34.

[29] R.H. Essenhigh, Symp. (Int.) Combust. 22 (1988) 89-96.

[30] G.A. Kelesidis, E. Goudeli, S.E. Pratsinis, Proc. Combust. Inst. 36 (2017) 29-50.

[31] F.E. Kruis, K.A. Kusters, S.E. Pratsinis, B. Scarlett, Aerosol Sci. Technol. 19 (1993) 514-526.

[32] Y. Xiong, S.E. Pratsinis, J. Aerosol Sci. 24 (1993) 283-300.

[33] D. Avnir, D. Farin, P. Pfeifer, Nature 308 (1984) 261-263.

[34] G.A. Kelesidis, M.R. Kholghy, J. Zuercher, J. Robertz, M. Allemann, A. Duric, S.E. Pratsinis, Powder Technol. 20 (2019) doi.org/10.1016/j.powtec.2019.02.003.

[35] M. Alfe, B. Apicella, R. Barbella, J.N. Rouzaud, A. Tregrossi, A. Ciajolo, Proc. Combust. Inst. 32 (2009) 697-704.

[36] H. Ghiassi, P. Toth, I.C. Jaramillo, J.S. Lighty, Combust. Flame 163 (2016) 179-187.

[37] K.O. Johansson, F. El Gabaly, P.E. Schrader, M.F. Campbell, H.A. Michelsen, Aerosol Sci. Technol. 51 (2017) 1333-1344.

[38] E.W. Thiele, Ind. Eng. Chem. 31 (1939) 916-920.

[39] I.C. Jaramillo, C.K. Gaddam, R.L. Vander Wal, C.H. Huang, J.D. Levinthal, J.S. Lighty, Combust. Flame 161 (2014) 2951-2965.

[40] W. Kast, C.R. Hohenthanner, Int. J. Heat Mass Trans. 43 (2000) 807-823.

[41] P. Grancic, J.W. Martin, D.P. Chen, S. Mosbach, M. Kraft, Carbon 109 (2016) 608-615.

[42] M.L. Eggersdorfer, A.J. Gröhn, C.M. Sorensen, P.H. McMurry, S.E. Pratsinis, J. Colloid Interf. Sci. 387 (2012) 12-23.

[43] R.A. Dobbins, R.A. Fletcher, H.C. Chang, Combust. Flame 115 (1998) 285-298.

[44] T.S. Totton, D. Chakrabarti, A.J. Misquitta, M. Sander, D.J. Wales, M. Kraft, Combust. Flame 157 (2010) 909-914.

[45] G.A. Kelesidis, S.E. Pratsinis, Proc. Combust. Inst. 37 (2019) 1177-1184.

[46] J. Camacho, C.R. Liu, C. Gu, H. Lin, Z. Huang, Q.X. Tang, X.Q. You, C. Saggese, Y. Li, H.J. Jung, L. Deng, I. Wlokas, H. Wang, Combust. Flame 162 (2015) 3810-3822.

[47] C. Betrancourt, F.S. Liu, P. Desgroux, X. Mercier, A. Faccinetto, M. Salamanca, L. Ruwe, K. Kohse-Höinghaus, D. Emmrich, A. Beyer, A. Golzhauserd, T. Tritscher, Aerosol Sci. Technol. 51 (2017) 916-935.

[48] F. Schulz, M. Commodo, K. Kaiser, G. De Falco, P. Minutolo, G. Meyer, A. D'Anna, L. Gross, Proc. Combust. Inst. 37 (2019) 885-892.

[49] E.L. Cussler, Diffusion: Mass transfer in Fluid Systems, Cambridge University Press, 1997.

[50] D.R. Warren, J.H. Seinfeld, J. Colloid Interf. Sci. 105 (1985) 136-142.

[51] M. Schenk, S. Lieb, H. Vieker, A. Beyer, A. Gölzhauser, H. Wang, K. Kohse-Höinghaus, ChemPhysChem 14 (2013) 3248-3254.

[52] K.B. Lee, M.W. Thring, J.M. Beer, Combust. Flame 6 (1962) 137-145.

[53] G.D.J. Guerrero Pena, M.M. Alrefaai, S.Y. Yang, A. Raj, J.L. Brito, S. Stephen, T. Anjana, V. Pillai, A. Al Shoaibi, S.H. Chung, Combust. Flame 172 (2016) 1-12.
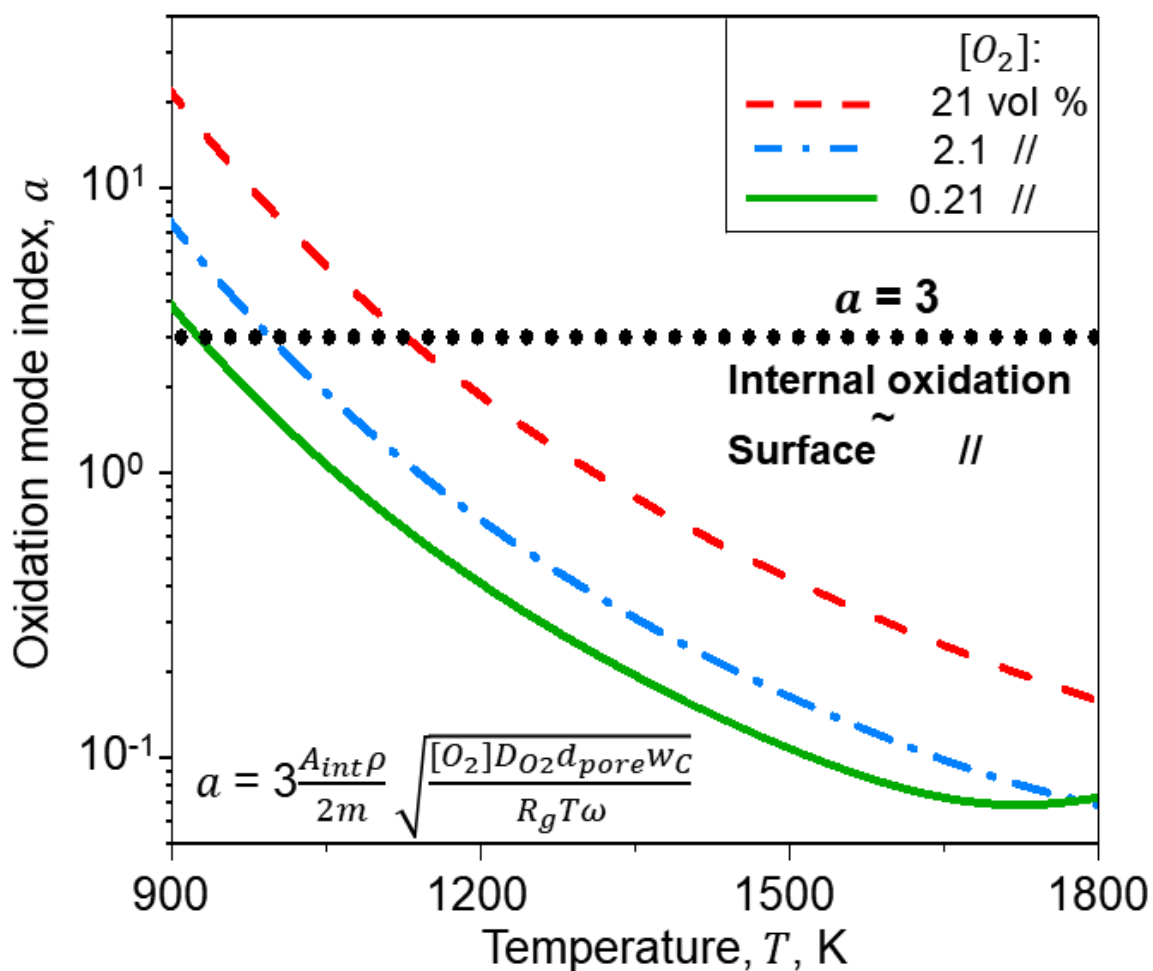
**Figures:**



**Figure 1.** Oxidation mode index, $a$, as function of temperature, $T$, for $O_2$ concentration, $[O_2]$ = 21 (broken line), 2.1 (dot-broken line) and 0.21 vol % (solid line) estimated using Eq. 10 with specific oxidation rate, $\omega$, for mature soot or carbon black derived by Nagle-Strickland-Constable [12; NSC] and $d_{va,o}$ = 16.7 nm [8]. For $a$ = 3 (dotted line), the contributions of internal and surface oxidation to the total oxidized soot mass are equal. The ratio of internal to surface oxidation decreases with increasing $T$ and decreasing $[O_2]$ reducing $\alpha$ below 3 making surface oxidation the dominant mechanism for soot oxidation.
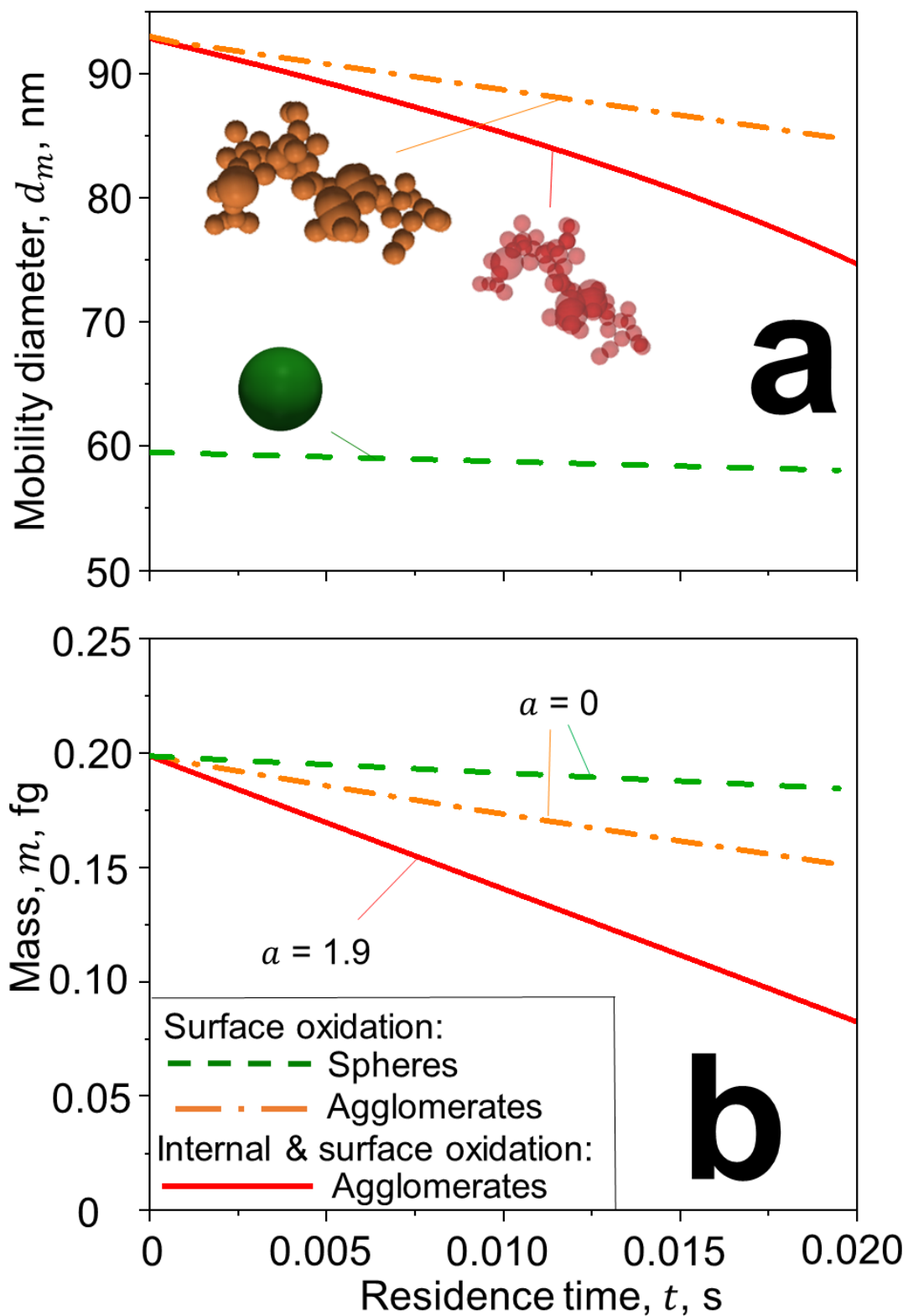
**Figure 2.** Evolutions of a) mobility diameter, $d_m$, and b) mass, $m$, of soot agglomerates by internal and surface oxidation (solid lines) in comparison to mere surface oxidation of agglomerates (dot-broken lines) and equivalent-mass spheres (broken lines). The agglomerate $d_m$ and $m$ decrease faster (dot-broken lines) than spheres (broken lines) due to the larger surface area of the former. Accounting for internal oxidation accelerates the reduction of the agglomerate $m$ and $d_m$ compared to that attained by surface oxidation alone.
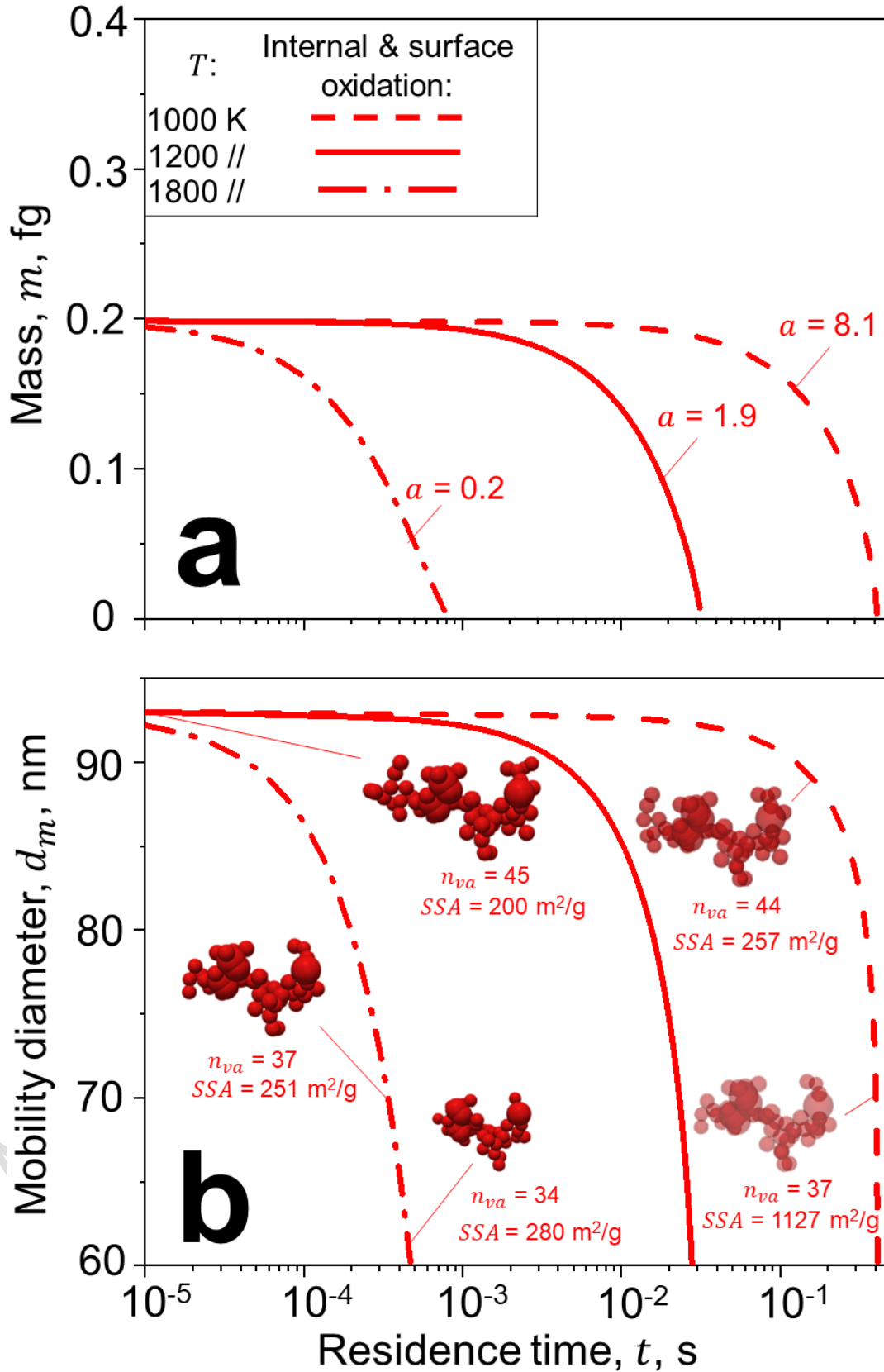
**Figure 3.** Evolution of a) $m$ and b) $d_m$ of soot agglomerates during internal and surface oxidation at $T = 1800$ (dot-broken lines), 1200 (solid lines) and 1000 K (broken lines) and $[O_2] = 21$ vol %. Surface oxidation becomes more dominant than internal burning with increasing $T$, decreasing $\alpha$ (Eq. 10; Fig. 1) and accelerating the reduction of $m$, $d_m$, number of primary particles per agglomerate, $n_{va}$, and specific surface area, $SSA$.
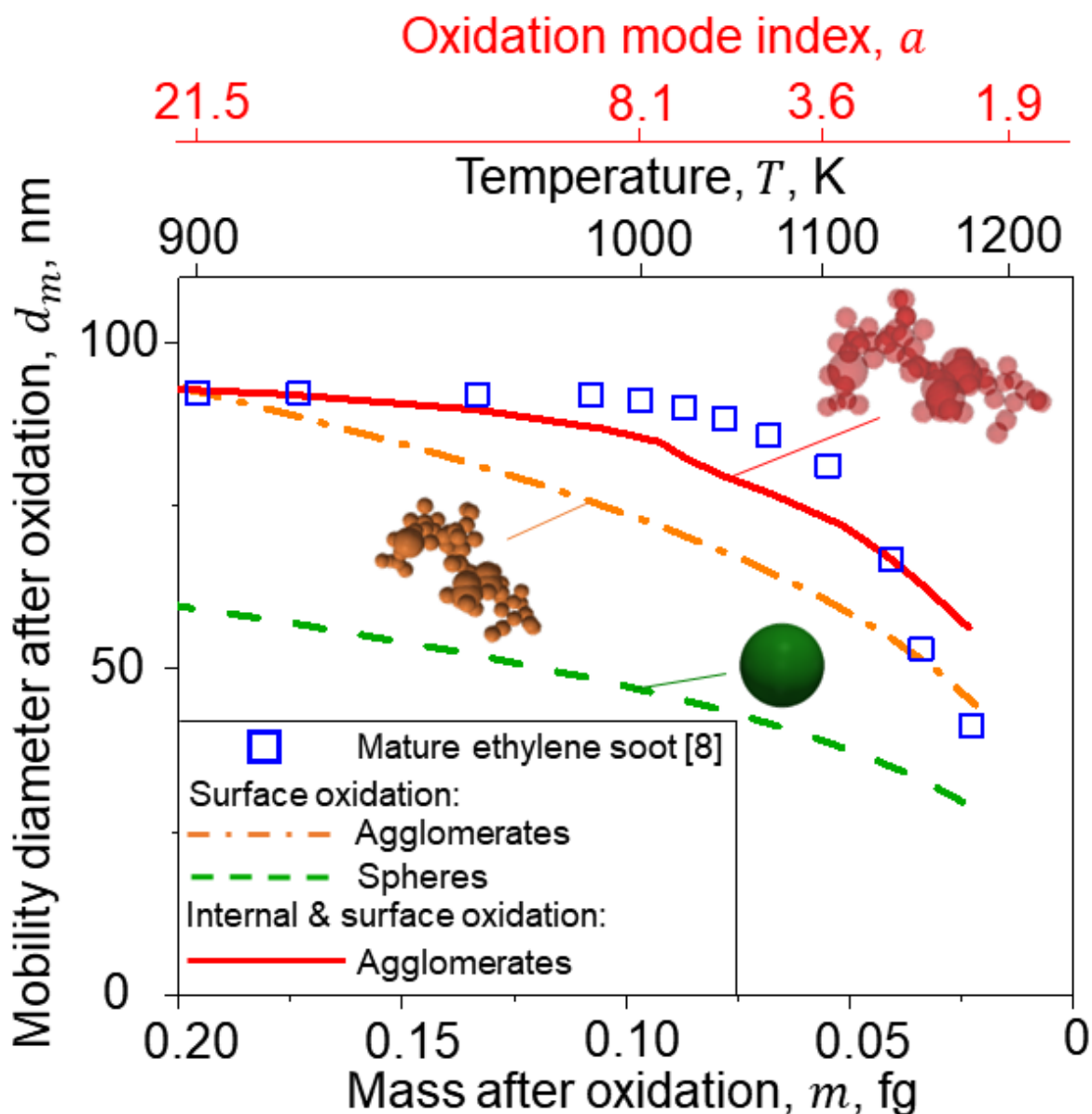
19

**Figure 4.** Soot agglomerate $d_m$ as function of its $m$ after internal and surface oxidation (solid line) at $T = 900 – 1200$ K (top axis) resulting in $a = 21.5 – 1.9$ (top axis) is compared to surface oxidation of spheres (broken line) and agglomerates (dot-broken line), as well as to mature ethylene soot oxidation data [8; squares]. The $d_m$ estimated by internal and surface oxidation of soot agglomerates (solid line) is in excellent agreement with the mature soot data [8; squares] in the whole $T$ range. The agglomerate $d_m$ attained by surface oxidation alone (dot-broken line) is in good agreement with data [8; squares] for $T > 1100$ K, but underestimates soot $d_m$ up to 24 % for lower $T$ for which internal oxidation is dominant [8]. Neglecting the fractal-like soot morphology (broken line) results in 50 % underestimation of the measured $d_m$ [8; squares] for the whole $T$ range.
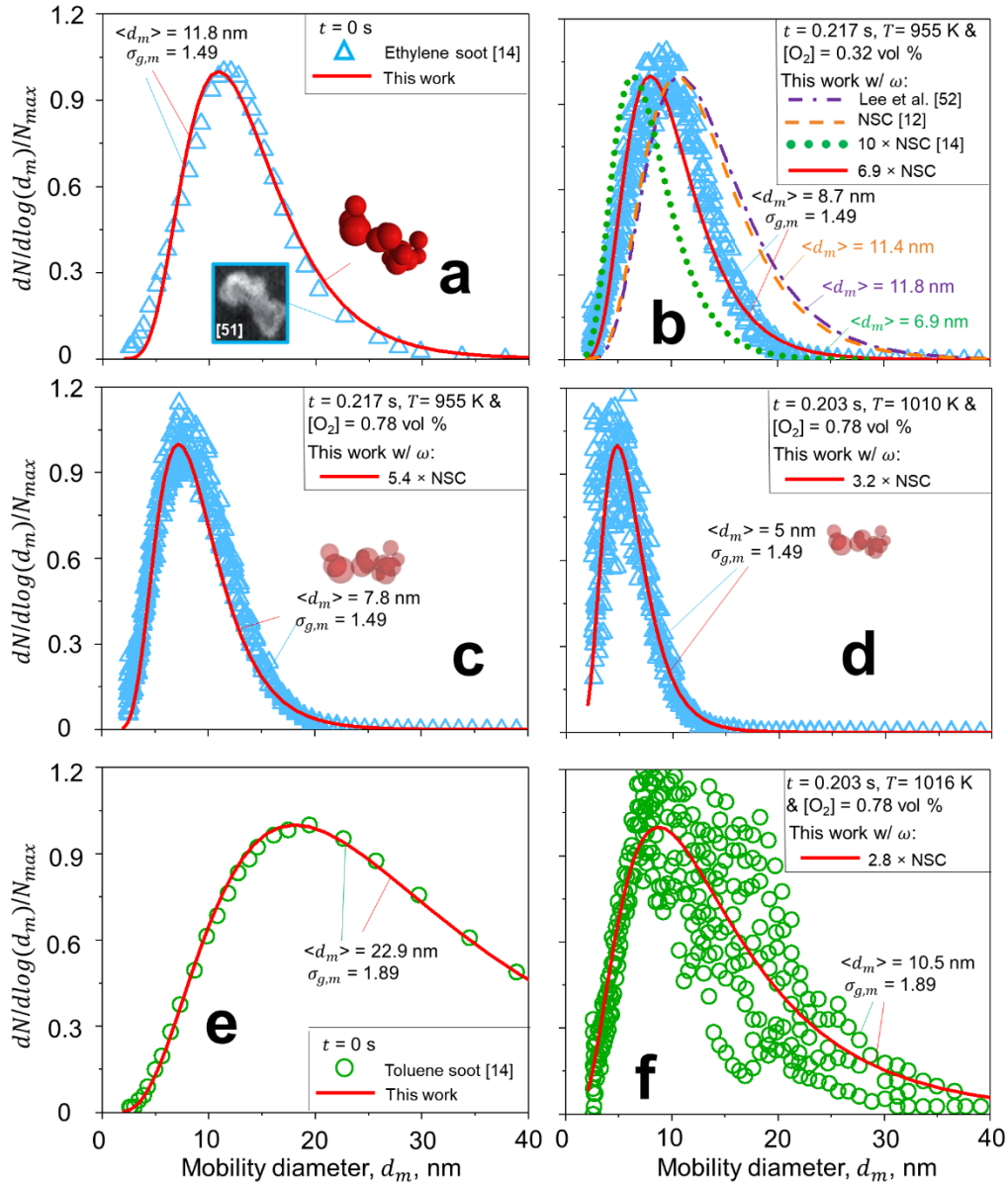
**Figure 5.** Normalized mobility size distributions of agglomerates before (a, e; $t = 0$ s) and after 0.217 (b, c) or 0.203 s (d, f) of internal and surface oxidation at $T = 955$ (b, c), 1010 K (d) or 1016 K (f) and $[O_2] = 0.32$ (b) or 0.78 vol % (c, d, f) obtained by a moving sectional model (lines) and compared to those measured during nascent ethylene [14; triangles] or toluene soot oxidation [14; circles]. At $t = 0$ s (a), soot nanoparticles form compact agglomerates of aggregates and single primary particles [51; blue-framed inset] by surface growth and agglomeration [3] having average $\langle d_m \rangle = 11.8$ nm and $\sigma_{g,m} = 1.49$ [14; triangles] or $\langle d_m \rangle = 22.9$ nm and $\sigma_{g,m} = 1.89$ [14; circles]. Using $\omega = $ NSC for mature carbon black [12] or a similar $\omega$ for mature soot [52] results in $\langle d_m \rangle = 11.4$ (b: broken line) and 11.8 nm (b: dot-broken line), respectively, which are 30 and 35 % larger than the measured $\langle d_m \rangle = 8.7$ nm after 0.217 s at $T = 955$ K and $[O_2] = 0.32$ vol % [14; triangles]. Using $\omega = 10 \times$ NSC derived for nascent soot spheres and cylinders [14] underestimates the measured $\langle d_m \rangle$ by 20 % (b: dotted line). Accounting for the detailed fractal-like soot structure and internal oxidation, the best agreement with the measured $\langle d_m \rangle$ [14; triangles] is attained with $\omega = 6.9 \times$ NSC (solid line). The underestimation of nascent ethylene soot oxidation rate by the NSC rate decreases down to $5.4 \times$ NSC or $3.2 \times$ NSC with increasing $[O_2]$ (c) or $T$ (d). Nascent toluene soot is less reactive than ethylene soot due to its large C/H ratio, resulting in 15 % smaller $\omega$ for similar $T$ and $[O_2]$ conditions (d, f).